

# Work function dependent photogenerated carrier dynamics of defective transition metal dichalcogenide heterostructures

Tingbo Zhang,<sup>1,\*</sup> Yehui Zhang,<sup>1,\*</sup> Xianghong Niu,<sup>2,†</sup> Qian Chen,<sup>1</sup> and Jinlan Wang<sup>1,‡</sup>

<sup>1</sup>Key Laboratory of Quantum Materials and Devices of Ministry of Education, School of Physics, Southeast University, Nanjing 21189, China

<sup>2</sup>New Energy Technology Engineering Laboratory of Jiangsu Province, School of Science, Nanjing University of Posts and Telecommunications, Nanjing 210023, China



(Received 28 June 2023; revised 3 October 2023; accepted 5 October 2023; published 30 October 2023; corrected 2 November 2023)

Vacancies are commonly introduced in the preparation of transition metal dichalcogenide (TMD) heterostructures, severely affecting photogenerated carrier dynamics. Herein, we systematically explore the carrier dynamics of TMD heterostructures (metal: Mo, W; chalcogen: S, Se, Te) with the most common chalcogen vacancies by nonadiabatic molecular dynamics simulations. For TMD monolayers, a chalcogen vacancy induces defect states around the conduction band minimum forming a recombination center, while in heterostructures, locations of defect states in different sublayers exhibit clear work function dependence. Specifically, the defect states of a sublayer with a high work function are pushed down and act as photogenerated carrier recombination centers, while those of a sublayer with a low work function are pushed up and defect tolerant. This is because the delocalized charge distribution weakens the overlap of photogenerated electrons and holes. This indicates that repairing the defects of sublayers with a high work function can eliminate the adverse effect of vacancies. As a further demonstration, oxygen passivation is employed to repair the defects of sublayers with a high work function, which fully recovers the 10 ns scale of the photogenerated carrier lifetime. In this paper, we provide an in-depth understanding of defective carrier dynamics and guidelines for high-performance TMD heterostructure photoelectric devices.

DOI: [10.1103/PhysRevB.108.165428](https://doi.org/10.1103/PhysRevB.108.165428)

## I. INTRODUCTION

Two-dimensional (2D) transition metal dichalcogenide (TMD) heterostructures have attracted broad attention in photovoltaics [1] and photoelectric devices [2–4] due to the characteristics of tunable band gap [5,6], valley degrees of freedom [7], and fast carrier separation [8–10]. Generally, defects are impossible to avoid during the experimental preparation of TMD heterostructures [11], which greatly affects the photoelectronic performance of 2D-based devices by affecting the carrier dynamics. [12–16]. For example, Wang *et al.* [17] and Zhu *et al.* [18] revealed that defects of TMD heterostructures are detrimental to the photoelectric properties due to defects acting as carrier recombination centers. Differently, Fu *et al.* [19] found that S vacancies in the WS<sub>2</sub> sublayer can improve the photoresponsivity of photodetectors, as they effectively trap hot electrons within the heterostructure. Hence, understanding and regulating the defect-related carrier dynamics in TMD heterostructures is of vital importance for the high-performance photoelectric devices.

Regarding defects of heterostructures, S, Se, and Te (named the S-family) vacancies are frequently observed [20,21]. Single-S vacancies in TMD monolayers

introduce localized defect states around the conduction band minimum (CBM), which may act as photogenerated carrier recombination centers [22–24]. However, for the case of double-S vacancies, the carrier lifetime is longer, probably arising from the redistribution of defect states due to the strong defect interactions [25]. Similarly, defect state locations of TMD heterostructures can be shifted by the synergistic interactions of defects in different sublayers and interfaces, resulting in a more complicated electronic structure [26–28]. It is commonly accepted that electronic structure is closely related to photogenerated carrier dynamics. More precisely, the change of defect state locations of heterostructures has a greater chance to induce the interlayer transfer of carriers, causing multichannel carrier recombination. Can all channels introduced by defects in different sublayers accelerate carrier recombination, or do only some channels bind photogenerated carriers to prolong electron-hole (e-h) lifetime, as observed in black phosphorus with phosphorus vacancies [29]? Limited by experimental conditions, the effect of these defect-induced channels in TMD heterostructures on carrier recombination is not clearly elucidated yet.

In this paper, combining first-principles calculations and nonadiabatic molecular dynamics (NAMD) simulations, we systematically study the influence of different S vacancies on photogenerated carrier dynamics of MoS<sub>2</sub>/WS<sub>2</sub> heterostructures. It is revealed that the carrier recombination through the S vacancy in the WS<sub>2</sub> sublayer is an order of magnitude slower than that through the S vacancy in the MoS<sub>2</sub> sublayer.

\*These authors contributed equally in this work.

†Second corresponding author: xhniu@njupt.edu.cn

‡First corresponding author: jlwang@seu.edu.cn

This may be attributed to the significant work function difference between sublayers, resulting in defect states of the WS<sub>2</sub> sublayer being higher than those of the MoS<sub>2</sub> sublayer. Meanwhile, the delocalized charge distribution at the valence band maximum (VBM) also weakens the overlap between the VBM and defect states of the WS<sub>2</sub> sublayer. Consequently, the S vacancy in the MoS<sub>2</sub> sublayer greatly accelerates the carrier recombination, while that in the WS<sub>2</sub> sublayer is defect tolerant. As a further demonstration, we try to repair the S vacancy in different sublayers and find that repairing the S vacancy in the MoS<sub>2</sub> sublayer via O<sub>2</sub> passivation increases the carrier lifetime by 5.6 times, while repairing the S vacancy in the WS<sub>2</sub> sublayer has little effect. Similar phenomena are also observed in other TMD heterostructures, suggesting the defect-related carrier dynamics mechanism and repairing strategy are of universality.

## II. COMPUTATIONAL METHODS

Density functional theory (DFT) was carried out for the static calculations of TMD heterostructures within the projector augmented-wave potentials as implemented in VASP [30,31]. The GGA-PBE functional was adopted to describe the exchange-correlation interaction [32–34]. The plane-wave cutoff energy was set to 450 eV, and the force was converged to 0.01 eV/Å. A Monkhorst-Pack k-point grid of  $5 \times 9 \times 1$  was adopted for the Brillouin zone integrations. The van der Waals interaction between TMD sublayers was included by Grimme *et al.* [35] (DFT-D2). A vacuum layer of  $> 15$  Å along the  $z$  axis was implemented to eliminate interaction between adjacent periods. Dipole correction was employed to cancel the potential errors of atomic force and total energy caused by periodic boundary conditions.

We studied photogenerated carrier dynamics using the Hefei-NAMD code based on the surface hopping approach [36–40]. Here, we provide a brief overview of the code. Time-dependent DFT (TDDFT) was employed to describe the electronic properties of the system:

$$\rho(\mathbf{r}, t) = \sum_{n=1}^{N_e} |\Psi_n(\mathbf{r}, t)|^2, \quad (1)$$

where  $\Psi_n(\mathbf{r}, t)$  represents the single-electron Kohn-Sham (KS) orbitals, and  $N_e$  stands for the number of electrons occupying the orbitals. By employing the time-dependent variational principle, we can derive a set of single-particle equations for the evolution of KS orbitals:

$$i\hbar \frac{\partial}{\partial t} \Psi_n(\mathbf{r}, t) = H(\mathbf{r}, \mathbf{R}, t) \Psi_n(\mathbf{r}, t). \quad (2)$$

The expansion of single-electron orbitals in the adiabatic KS orbital basis is given by

$$\Psi_n(\mathbf{r}, t) = \sum_k c_{nk}(t) |\varphi_k(\mathbf{r}; \mathbf{R})\rangle. \quad (3)$$

Substituting Eq. (3) into Eq. (2) yields the evolution equation for the expansion coefficients:

$$i\hbar \frac{\partial}{\partial t} c_j(t) = \sum_k c_{nk}(t) (\varepsilon_k \delta_{jk} + d_{jk}), \quad (4)$$

where  $\varepsilon_k$  represents the energy of the adiabatic KS state  $k$ . The nonadiabatic coupling can be expressed as follows:

$$\begin{aligned} d_{jk} &= -i\hbar \langle \varphi_j(\mathbf{r}; \mathbf{R}) | \nabla_{\mathbf{R}} | \varphi_k(\mathbf{r}; \mathbf{R}) \rangle \frac{d\mathbf{R}}{dt} \\ &= -i\hbar \left\langle \varphi_j(\mathbf{r}; \mathbf{R}) \left| \frac{\partial \varphi_k(\mathbf{r}; \mathbf{R})}{\partial t} \right. \right\rangle. \end{aligned} \quad (5)$$

In condensed matter systems, a mixed quantum-classical method is used to deal with NAMD. With this framework, nuclei are treated as classical particles, while electrons are treated as quantum particles. Coupling between nuclei and electrons is addressed through the surface hopping. Specifically, classical particles move along individual potential energy surfaces. The evolution of the electron wave function can hop between different potential energy surfaces. To enhance computational efficiency, Tully [38] proposed the method of fewest switches surface hopping. The hopping probabilities of electronic states  $j$  and  $k$  with the time interval  $dt$  can be written as

$$dP_{jk} = \frac{2\Re(a_{jk}^* d_{jk} \dot{\mathbf{R}})}{a_{jj}} dt; \quad jk = c_j^* c_k, \quad (6)$$

where  $a_{jk}$  is the element in density matrix of wave function expansion coefficients  $c_j$  and  $c_k$ . Here,  $d_{jk}$  is the first-order nonadiabatic coupling vector, and  $\dot{\mathbf{R}}$  is the nuclear velocity.

Initially, the states of the system are in a coherent state. These electronic states will maintain their coherence in the absence of external influences. However, external perturbations cause these coherent states to collapse onto a single electronic state. The process is known as quantum decoherence. For excited-state carrier dynamics processes with a long lifetime, as coherences vanish on the femtosecond time scale, it becomes necessary to apply decoherence corrections for surface hopping method. Based on this, Jaeger *et al.* [41] proposed the DISH. In this framework, decoherence time of each electronic state is determined through the solution of the Schrödinger equation. Subsequently, a random number is generated according to a Poisson distribution. If the random number surpasses the time of the most recent decoherence from a certain state, the system undergoes decoherence. The NAMD simulation process is as follows. After the geometry optimization, the temperature of TMD heterostructures was brought to 300 K. Then a 5 ps microcanonical trajectory and corresponding wave function were generated using *ab initio* molecular dynamics calculations, employing a time step of 1 fs. The nonadiabatic coupling (NAC) was derived from the wave function of molecular dynamics (MD) trajectory. In the e-h recombination process, we chose 50 initial configurations at the first 1 ps and used 500 random number sequences to execute surface hopping.

## III. RESULTS AND DISCUSSION

TMD (metal: Mo, W; chalcogen: S, Se, Te) monolayers can form 15 TMD heterostructures, among which the MoS<sub>2</sub>/WS<sub>2</sub> heterostructure is the most widely concerned in experiments [42,43]. Therefore, we chose the most stable stacking [AB1 in Fig. 1(a)] of the MoS<sub>2</sub>/WS<sub>2</sub> heterostructure to study carrier dynamics [44,45]. To distinguish it from a

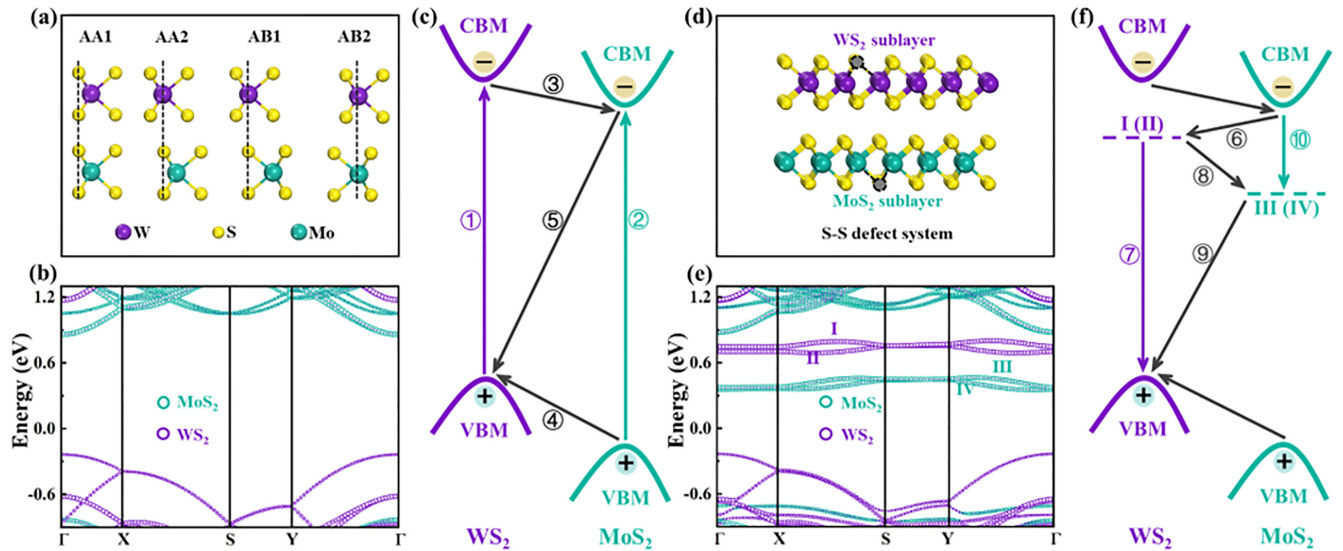


FIG. 1. Stacking configurations of (a) MoS<sub>2</sub>/WS<sub>2</sub> heterostructure and (d) S-S heterostructure. Band structures of (b) Perf and (e) S-S heterostructures. I–VI in (e) refer to different electron trapping states. Mechanism of e-h transfer and recombination of (c) Perf and (f) S-S heterostructures. ① and ② in (c) refer to generation of photogenerated carriers. ③–⑤ in (c) refer to transfer and recombination of electrons and holes. ⑥–⑩ in (f) refer to electron transfer process among conduction band minimum (CBM), defect states, and valence band maximum (VBM).

perfect heterostructure without defects (Perf), the heterostructure with S vacancies is named the S-S heterostructure. Meanwhile, S vacancies can be located on the outer and inner sides of different sublayers. Our calculations show that the defect formation energy of the outer one is the lowest (Fig. S1 and Table S1 in the Supplemental Material [46]); therefore, the S-S heterostructure refers to S vacancies on the outer side of the heterostructure, as shown in Fig. 1(d).

### A. Electronic structure

As displayed in Figs. 1(b) and 1(e), Perf and S-S heterostructures show type-II band alignment. The CBM of the heterostructures resides on the MoS<sub>2</sub> sublayer, while the VBM of the heterostructures has strong orbital hybridization (in Fig. S2 in the Supplemental Material [46]). The VBM charge distribution of the heterostructures is delocalized in both sublayers, consistent with previous work [44]. For the S-S heterostructure, the S-S defect introduces four electron trapping states (I–VI) below the CBM in Fig. 1(e), and their charge distribution is localized around the S vacancies in Figs. S2(b)–S2(d) in the Supplemental Material [46]. More precisely, I and II contributed by the WS<sub>2</sub> sublayer, close to the CBM of the heterostructure, are shallow defect states, while III and VI contributed by the MoS<sub>2</sub> sublayer, having a large difference with the CBM ( $\sim 0.51$  eV), are deep defect states. Such complicated electronic structures related to defect states may provide more channels for photogenerated carrier recombination [47]. Specifically, since the work function difference between MoS<sub>2</sub> and WS<sub>2</sub> sublayers shifts up the defect states of the WS<sub>2</sub> sublayer, the defect-associated carrier dynamics of the WS<sub>2</sub> sublayer may be different from that of the MoS<sub>2</sub> sublayer. Therefore, the effect of defect states in different sublayers on carrier recombination is elaborated in the next section.

## B. Photogenerated carrier transfer and recombination

### 1. Carrier dynamics of Perf heterostructure

Fast carrier interlayer transfer and slow interlayer recombination of the Perf heterostructure are observed, as shown in Figs. 1(c) and S4(a) in the Supplemental Material [46]. Specifically, the electron (③) and hole (④) transfer times are 111 and 329 fs, respectively. This is consistent with experimental results that the photogenerated carrier interlayer transfer time of TMD heterostructures is on the order of femtoseconds [48–50]. Meanwhile, the interlayer e-h recombination, as indicated by the 1.73% within 1000 ps (⑤) (see Fig. S3(a) in the Supplemental Material [46]), suggests that the carrier lifetime is at the nanosecond scale. This is beneficial to improve the performance of photoelectric devices.

The above results can be rationalized by NAC. The large NAC, resulting from the small energy gap, corresponds to the fast carrier transfer and the short carrier lifetime [51–54]. In this regard, the energy gaps of interlayer transfer ③ and ④ are 0.34 and 0.59 eV, respectively,  $\ll 1.09$  eV of interlayer recombination ⑤. A smaller energy gap reduces the energy barrier of carrier transition between different energy levels, leading to notably larger NAC of ③ and ④ (several millielectronvolts) than ⑤ (0.29 meV) in Fig. S3(c) in the Supplemental Material [46]. This incremental NAC promotes the carrier transfer between different energy levels.

### 2. Carrier dynamics of S-S heterostructure

For the S-S heterostructure, S vacancies introduce four electron trapping states, resulting in a more complicated e-h recombination process than the Perf heterostructure. This complexity is associated with four distinct channels, as depicted in Fig. 1(f). (i) Electrons in the CBM may directly recombine with holes in the VBM (⑩). (ii) Due to the energy level proximity, electrons in the CBM may first transfer to

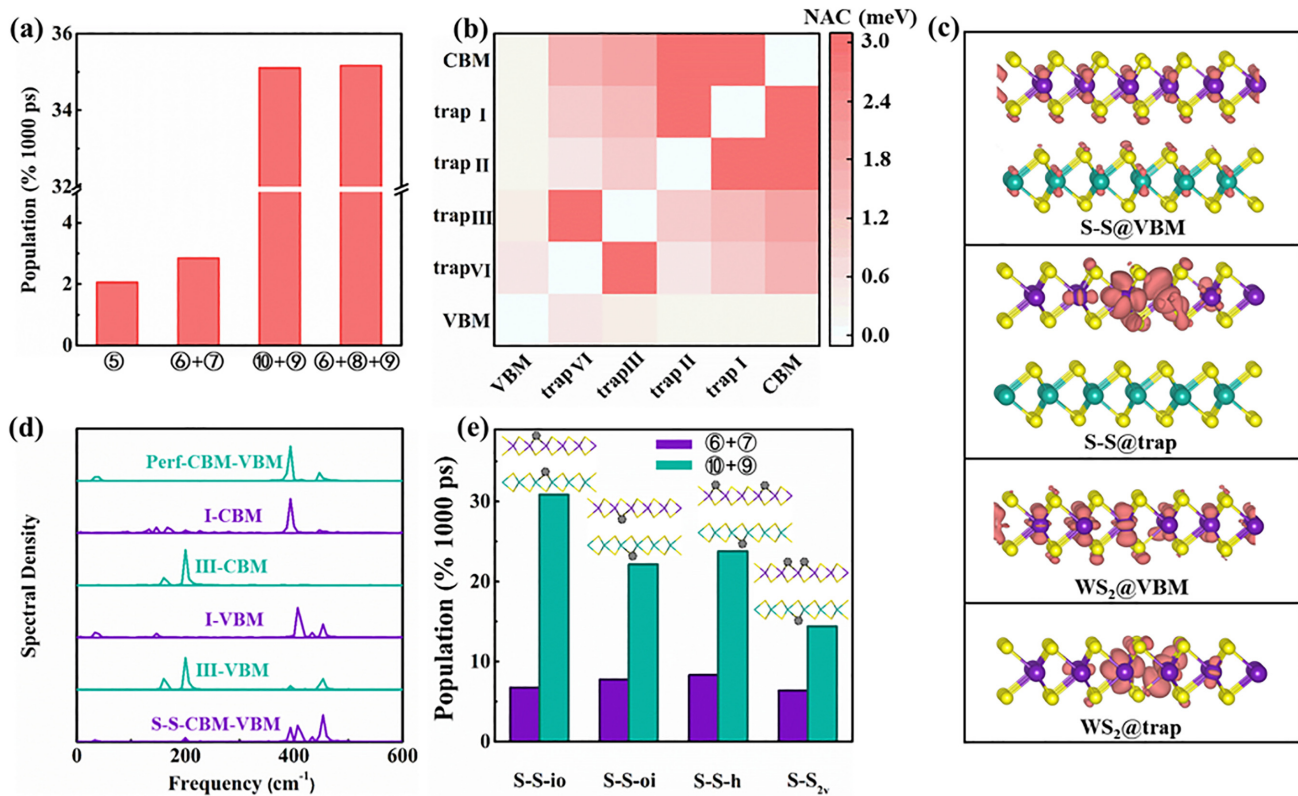


FIG. 2. (a) e-h recombination within 1000 ps of different processes for S-S heterostructure. (b) Nonadiabatic coupling (NAC) of S-S heterostructure. (c) Charge densities of S-S heterostructure at valence band maximum (VBM) and trap I (named as S-S@VBM and S-S@trap), WS<sub>2</sub> monolayer at VBM and S vacancy (named as WS<sub>2</sub>@VBM and WS<sub>2</sub>@trap). The isosurface value is  $2.0 \times 10^{-3} \text{ eV/\AA}^3$ . (d) Fourier transform (FT) spectrum of the autocorrelation function for Perf and S-S heterostructures in conduction band minimum (CBM), VBM, and defect states. (e) e-h recombination of different processes for S-S-io, S-S-oi, S-S-h, and S-S<sub>v</sub>. Insets are corresponding atomic structures with different locations, concentrations, and types of S vacancies, and gray balls represent vacancies.

defect states of the WS<sub>2</sub> sublayer and then recombine with holes in the VBM (⑥ + ⑦). (iii) Since the CBM is mainly contributed by the MoS<sub>2</sub> sublayer, electrons in the CBM may first transfer to defect states of the MoS<sub>2</sub> sublayer, followed by recombination with holes in the VBM (⑩ + ⑨). (iv) Owing to the interaction of defect states, electrons in the CBM may first transfer to defect states of the WS<sub>2</sub> sublayer, subsequently to defect states of the MoS<sub>2</sub> sublayer, and eventually recombine with holes in the VBM (⑥ + ⑧ + ⑨). For verification, we performed carrier dynamics simulations considering all these processes. As shown in Fig. 2(a), the carrier recombination of ⑩ + ⑨ (35.10%), like ⑥ + ⑧ + ⑨ (35.16%), is much faster than that of ⑥ + ⑦ (2.84%) within 1000 ps. Obviously, the S vacancy in the MoS<sub>2</sub> sublayer (⑩ + ⑨) is served as the photogenerated carrier recombination center, while the S vacancy in the WS<sub>2</sub> sublayer (⑥ + ⑦) is defect tolerant. Moreover, the interlayer recombination (⑤) of the S-S heterostructure is 2.05%, close to the perfect heterostructure (1.73%), indicating that ⑤ contributes little to the carrier recombination. Therefore, the defect assistance processes (⑩ + ⑨ and ⑥ + ⑧ + ⑨) are the main channels of photogenerated carrier recombination, consistent with the experimental results [50,55].

The above phenomena can be understood considering the NAC values. In general, a small energy gap and large electron-phonon (e-ph) coupling lead to large NAC [52]. For ⑩ + ⑨, the energy gap between the VBM and trapping state III

(IV) is smaller than that between the VBM and trapping state I (II) [see Fig. 1(d)]. Therefore, the NAC of the VBM with trapping state III (0.44 meV) is higher than that with trapping state I (0.29 meV), as shown in Fig. 2(b). This discrepancy promotes the carrier transfer from the trapping state III of the MoS<sub>2</sub> sublayer to the VBM. Furthermore, Fourier transform (FT) spectra of the autocorrelation function for Perf and heterostructures in the CBM, VBM, and defect states indicate that the S-S defect introduces a few impurity phonon modes. This can increase the e-ph coupling of ⑩ + ⑨, as shown in Fig. 2(d). Specifically, the S vacancy in the MoS<sub>2</sub> sublayer introduces impurity phonon modes  $\sim 160$  and  $206 \text{ cm}^{-1}$ , which can be assigned to the transverse acoustic (TA) mode ( $\sim 155 \text{ cm}^{-1}$ ) and longitudinal acoustic (LA) mode ( $\sim 220 \text{ cm}^{-1}$ ), respectively [56,57]. These provide more channels for e-ph coupling [58], thereby accelerating carrier recombination.

For ⑥ + ⑦, compared with WS<sub>2</sub>@VBM, charges at the VBM of the heterostructure (S-S@VBM) are found to be delocalized in the WS<sub>2</sub> and MoS<sub>2</sub> sublayers [Fig. 2(c)], which weakens the e-ph coupling between the VBM and defect states I (II). Therefore, the S vacancy, originally acting as the recombination center of the WS<sub>2</sub> monolayer, is no longer the main channel of the carrier recombination for the heterostructure [25]. In addition, compared with the Perf heterostructure (14.86 fs), the S-S heterostructure has a

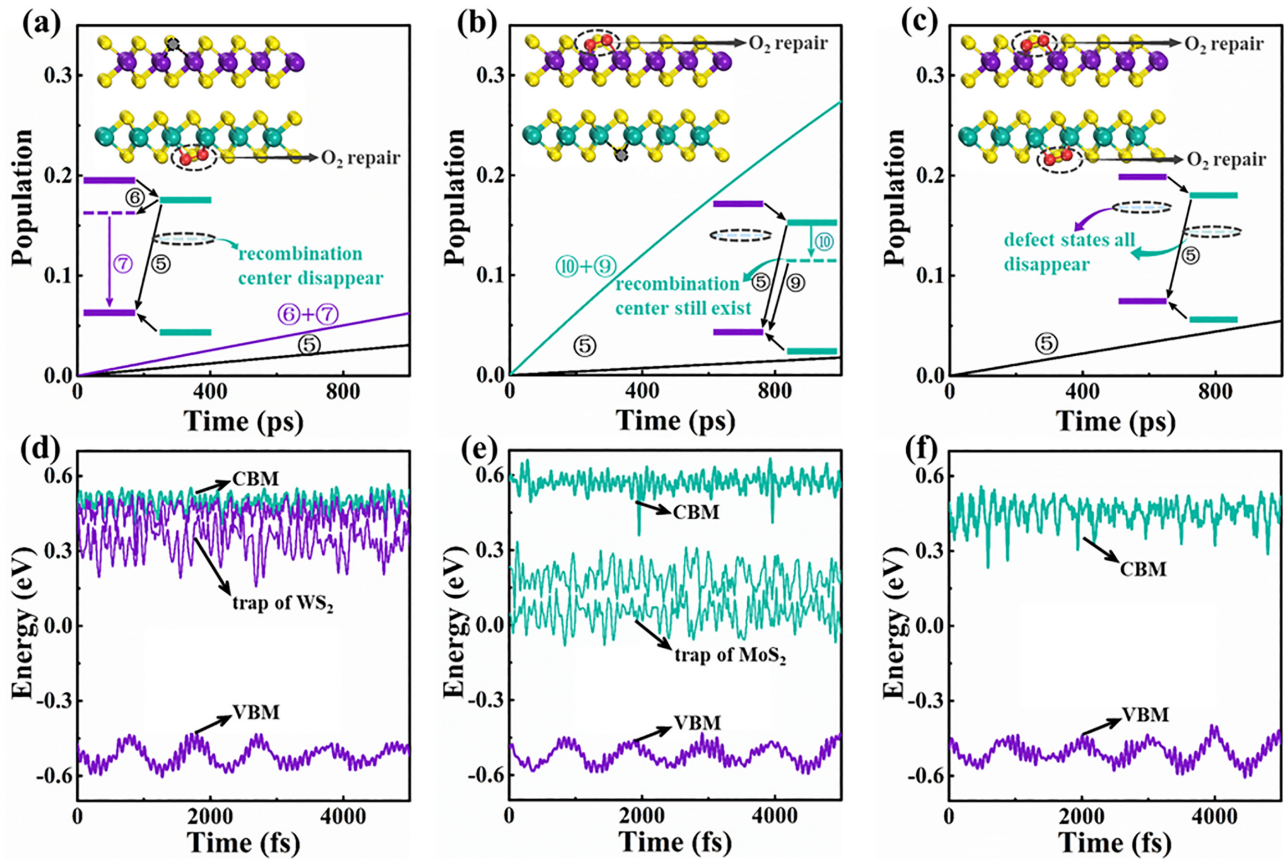


FIG. 3. e-h recombination different processes of (a) O-Mo, (b) O-W, and (c) O-Mo-W. Inset is corresponding atomic structure and mechanism of e-h recombination for O<sub>2</sub> repairing heterostructures. ⑤-⑩ of inset refer to electron transfer process among conduction band minimum (CBM), defect states, and valence band maximum (VBM). Time evolution of energy levels for (d) O-Mo, (e) O-W, and (f) O-Mo-W.

smaller pure-dephasing time, as shown in Fig. S3(d) in the Supplemental Material [46]. Generally, small pure-dephasing time corresponds to a long carrier lifetime [51], which means that the pure-dephasing time of the S-S heterostructure does not play a decisive role in affecting the e-h recombination.

The above studies have demonstrated that the S vacancy in the MoS<sub>2</sub> sublayer is the main channel of carrier recombination, while the S vacancy in the WS<sub>2</sub> sublayer is tolerant. To further verify this conclusion, we consider different locations, concentrations, and types of S vacancies, and their structures and e-h recombinations are presented in Fig. 2(e). Specifically, when changing locations of S vacancies in heterostructures (S-S-io and S-S-oi), they all have similar electronic structures to the S-S heterostructure (Fig. S4 in the Supplemental Material [46]). Thus, the e-h recombination is mainly through the S vacancy in the MoS<sub>2</sub> sublayer (⑩ + ⑨). In addition, we increase the S vacancy concentration of the WS<sub>2</sub> sublayer (S-S-h). As shown in Fig. S4(c) in the Supplemental Material [46], although it introduces more electron trapping states, they are all close to the CBM, acting as shallow defect states. Defect states introduced by the S vacancy in the MoS<sub>2</sub> sublayer retain deep defect states, functioning as the recombination center (⑩ + ⑨). A similar phenomenon is observed for the case of disulfide vacancy in the WS<sub>2</sub> sublayer (S-S<sub>2v</sub>) as well. In a word, the defect-related dynamics of the MoS<sub>2</sub>/WS<sub>2</sub> heterostructure show clear work function dependence. That

is, the S vacancy in the MoS<sub>2</sub> sublayer with a high work function is always the carrier recombination center, while the S vacancy in the WS<sub>2</sub> sublayer with a low work function is defect tolerant.

Tracing the source, it is because the different work functions of the sublayers alter the defect state locations and introduce delocalized charge distribution at the VBM of the heterostructure. On one hand, due to the relatively lower work function [59], defect states of the WS<sub>2</sub> monolayer are positioned closer to the CBM of the heterostructure. As a result, these defect states are shallow in the heterostructure and have a more significant energy gap with the VBM. On the other hand, charges at the VBM of the heterostructure are delocalized in the WS<sub>2</sub> and MoS<sub>2</sub> sublayers, weakening the e-ph coupling between defect states and the VBM. This leads to smaller NAC between defect states of the WS<sub>2</sub> sublayer and the VBM. Therefore, the S vacancy in the WS<sub>2</sub> sublayer is not served as the recombination center. Meanwhile, the defect states of the MoS<sub>2</sub> sublayer are near the middle of the band gap of the heterostructure. The deep defect states make ⑩ + ⑨ become the main channel for carrier recombination.

### 3. Repairing vacancies

Clearly, the S vacancy in the MoS<sub>2</sub> sublayer always accelerates the e-h recombination, while that in the WS<sub>2</sub> sublayer

is defect tolerant. That is, just repairing partial S vacancies has a chance to achieve long carrier lifetime. To verify this point, we investigate the influence of O<sub>2</sub> repairing of S vacancies of different sublayers on the carrier recombination. As expected, after O<sub>2</sub> repairing the S vacancy in MoS<sub>2</sub>, it restores the long carrier lifetime of the heterostructure (see Figs. 3(a) and S3(a) in the Supplemental Material [46]). More precisely, as shown in Figs. 3(a), 3(b), 3(d), and 3(e), after the S vacancy in the MoS<sub>2</sub> or WS<sub>2</sub> sublayer (O-Mo or O-W) is repaired, deep (shallow) defect states of the MoS<sub>2</sub> (WS<sub>2</sub>) sublayer vanish. The carrier recombination within 1000 ps of O-Mo (6.25%) is smaller than that of O-W (28.97%). Further, we study the electronic structure and carrier recombination of repairing S vacancies in MoS<sub>2</sub> and WS<sub>2</sub> sublayers through O<sub>2</sub> (O-Mo-W) in Figs. 3(c) and 3(f). Deep and shallow defect states of MoS<sub>2</sub> and WS<sub>2</sub> sublayers all vanish after O<sub>2</sub> repairing. Note that only 5.46% of electrons for O-Mo-W are recombined within 1000 ps, like the O-Mo heterostructure (6.25%). That is, only repairing the S vacancy in the MoS<sub>2</sub> sublayer with O<sub>2</sub> can significantly weaken the carrier recombination. Thus, the S vacancy in the WS<sub>2</sub> sublayer can be ignored, which is cost effective and reduces the difficulty of fabrication in experiment.

### C. Generality

TMD heterostructures consisting of TMD (metal: Mo, W; chalcogen: S, Se, Te) monolayers have 15 types. Considering the lattice mismatch, six TMD heterostructures (MoSe<sub>2</sub>/WSe<sub>2</sub>, MoTe<sub>2</sub>/WTe<sub>2</sub>, MoS<sub>2</sub>/WSe<sub>2</sub>, MoSe<sub>2</sub>/WS<sub>2</sub>, MoS<sub>2</sub>/MoSe<sub>2</sub>, and WS<sub>2</sub>/WSe<sub>2</sub>) are selected to further demonstrate the generality of defect-related carrier dynamics mechanism and repairing strategy.

The above six perfect heterostructures all have type-II band alignment (Fig. S5 in the Supplemental Material [46]). Defect states of sublayers with a high work function are all near the middle of the band gap of the heterostructures, while those with a low work function are near the CBM or located above the CBM (see Fig. 4). It can be inferred that defects of sublayers with a high work function can accelerate the carrier recombination, while those with a low work function are defect tolerant. Meanwhile, O<sub>2</sub> repaired sublayers with a high work function can eliminate carrier recombination centers (see Figs. S5 and S6 in the Supplemental Material [46]). This demonstrates the defect-related carrier dynamics mechanism and repairing strategy are universal. In addition, for four (MoS<sub>2</sub>/WSe<sub>2</sub>, MoSe<sub>2</sub>/WS<sub>2</sub>, MoS<sub>2</sub>/MoSe<sub>2</sub>, and WS<sub>2</sub>/WSe<sub>2</sub>) heterostructures, defect states of sublayers with a low work function are pushed above the CBM in Figs. 4(c)–4(j), which may be due to the synergistic effect of the work function difference and the electrostatic potential difference. Consequently, defect states of sublayers with a lower work function no longer provide additional channels for carrier recombination. Moreover, like the MoS<sub>2</sub>/WS<sub>2</sub> heterostructure, only repairing vacancies in sublayers with a high work function through O<sub>2</sub> can eliminate defect states inside the band gap for four heterostructures (Figs. S6 and S7 in the Supplemental Material [46]), which can obtain long-lifetime photogenerated carriers. Thus, we can search for sublayers with large electrostatic potential differences to construct heterostructures to realize long carrier lifetime devices.

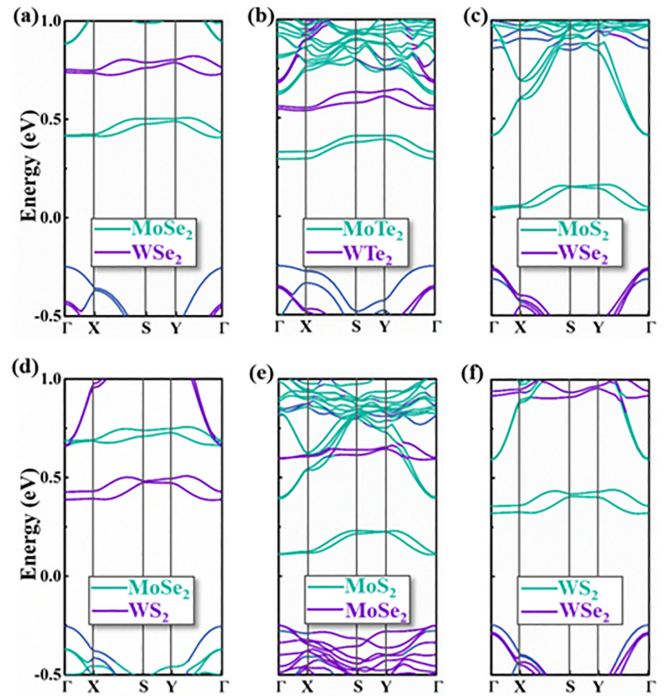


FIG. 4. Band structures of (a) MoSe<sub>2</sub>/WSe<sub>2</sub>, (b) MoTe<sub>2</sub>/WTe<sub>2</sub>, (c) MoS<sub>2</sub>/WSe<sub>2</sub>, (d) MoSe<sub>2</sub>/WS<sub>2</sub>, (e) MoS<sub>2</sub>/MoSe<sub>2</sub>, and (f) WS<sub>2</sub>/WSe<sub>2</sub> heterostructures with S-family vacancies in different sublayers.

## IV. CONCLUSIONS

In summary, combining first-principles calculations and NAMD simulations, we have studied the effects of different S-family vacancy defects on photogenerated carrier dynamics of TMD heterostructures and revealed the mechanism of work function-dependent carrier dynamics in defective heterostructures. S vacancies in sublayers with a low work function can be tolerant, while those in sublayers with a high work function are the carrier recombination centers, independent of location, concentration, and type of S vacancies. This can be attributed to the defect state movement caused by the work function difference between sublayers and the electrostatic potential difference. Furthermore, carrier recombination centers of heterostructures are effectively eliminated by O<sub>2</sub> repairing S vacancies in sublayers with a high work function. On these bases, two possible strategies for facile fabrication of high-photovoltaic-performance TMD heterostructure devices are therefore suggested for experiments: (i) try to avoid or repair S-family vacancies in sublayers with a high work function, and (ii) search for sublayers with large electrostatic potential differences to construct the heterostructure.

## ACKNOWLEDGMENTS

This paper was supported by the National Key Research and Development Program of China (Grant No. 2022YFA3807200), National Natural Science Foundation of China (Grants No. 22033002, No. 21525311, and No. 21973011), and the Basic Research Program of Jiangsu

Province (Grant No. BK20222007). The authors acknowledge the computational resources from the Big Data Computing

Center of Southeast University and National Supercomputing Center of Tianjin.

- [1] L. A. Jauregui, A. Y. Joe, K. Pistunova, D. S. Wild, A. A. High, Y. Zhou, G. Scuri, K. De Greve, A. Sushko, C. H. Yu *et al.*, Electrical control of interlayer exciton dynamics in atomically thin heterostructures, *Science* **366**, 870 (2019).
- [2] M. H. Doan, Y. Jin, S. Adhikari, S. Lee, J. Zhao, S. C. Lim, and Y. H. Lee, Charge transport in MoS<sub>2</sub>/WSe<sub>2</sub> van der Waals heterostructure with tunable inversion layer, *ACS Nano* **11**, 3832 (2017).
- [3] P. Rivera, H. Yu, K. L. Seyler, N. P. Wilson, W. Yao, and X. Xu, Interlayer valley excitons in heterobilayers of transition metal dichalcogenides, *Nat. Nanotechnol.* **13**, 1004 (2018).
- [4] X. Hong, J. Kim, S. F. Shi, Y. Zhang, C. Jin, Y. Sun, S. Tongay, J. Wu, Y. Zhang, and F. Wang, Ultrafast charge transfer in atomically thin MoS<sub>2</sub>/WS<sub>2</sub> heterostructures, *Nat. Nanotechnol.* **9**, 682 (2014).
- [5] A. Varghese, D. Saha, K. Thakar, V. Jindal, S. Ghosh, N. V. Medhekar, S. Ghosh, and S. Lodha, Near-direct bandgap WSe<sub>2</sub>/ReS<sub>2</sub> Type-II pn heterojunction for enhanced ultrafast photodetection and high-performance photovoltaics, *Nano Lett.* **20**, 1707 (2020).
- [6] P. Zereszki, P. Yao, D. He, Y. Wang, and H. Zhao, Interlayer charge transfer in ReS<sub>2</sub>/WS<sub>2</sub> van der Waals heterostructures, *Phys. Rev. B* **99**, 195438 (2019).
- [7] C. Jin, J. Kim, M. I. B. Utama, E. C. Regan, H. Kleemann, H. Cai, Y. Shen, M. J. Shinner, A. Sengupta, K. Watanabe *et al.*, Imaging of pure spin-valley diffusion current in WS<sub>2</sub>-WSe<sub>2</sub> heterostructures, *Science* **360**, 893 (2018).
- [8] R. Long and O. V. Prezhdo, Quantum coherence facilitates efficient charge separation at a MoS<sub>2</sub>/MoSe<sub>2</sub> van der Waals junction, *Nano Lett.* **16**, 1996 (2016).
- [9] Y. Liang, J. Li, H. Jin, B. Huang, and Y. Dai, Photoexcitation dynamics in Janus-MoSSe/WSe<sub>2</sub> heterobilayers: *Ab initio* time-domain study, *J. Phys. Chem. Lett.* **9**, 2797 (2018).
- [10] G. H. Shin, C. Park, K. J. Lee, H. J. Jin, and S. Y. Choi, Ultra-sensitive phototransistor based on WSe<sub>2</sub>-MoS<sub>2</sub> van der Waals heterojunction, *Nano Lett.* **20**, 5741 (2020).
- [11] Y. Gong, S. Lei, G. Ye, B. Li, Y. He, K. Keyshar, X. Zhang, Q. Wang, J. Lou, Z. Liu *et al.*, Two-step growth of two-dimensional WSe<sub>2</sub>/MoSe<sub>2</sub> heterostructures, *Nano Lett.* **15**, 6135 (2015).
- [12] C. Tan and H. Zhang, Epitaxial growth of hetero-nanostructures based on ultrathin two-dimensional nanosheets, *J. Am. Chem. Soc.* **137**, 12162 (2015).
- [13] P. Liu and B. Xiang, 2D hetero-structures based on transition metal dichalcogenides: Fabrication, properties and applications, *Sci. Bull.* **62**, 1148 (2017).
- [14] P. Merkl, F. Mooshammer, P. Steinleitner, A. Girnghuber, K. Q. Lin, P. Nagler, J. Holler, C. Schuller, J. M. Lupton, T. Korn *et al.*, Ultrafast transition between exciton phases in van der Waals heterostructures, *Nat. Mater.* **18**, 691 (2019).
- [15] N. T. Duong, S. Bang, S. M. Lee, D. X. Dang, D. H. Kuem, J. Lee, M. S. Jeong, and S. C. Lim, Parameter control for enhanced peak-to-valley current ratio in a MoS<sub>2</sub>/MoTe<sub>2</sub> van der Waals heterostructure, *Nanoscale* **10**, 12322 (2018).
- [16] A. Pezeshki, S. H. Shokouh, T. Nazari, K. Oh, and S. Im, Electric and photovoltaic behavior of a few-layer  $\alpha$ -MoTe<sub>2</sub>/MoS<sub>2</sub> dichalcogenide heterojunction, *Adv. Mater.* **28**, 3216 (2016).
- [17] J. Wang, J. Ardelean, Y. Bai, A. Steinhoff, M. Florian, F. Jahnke, X. Xu, M. Kira, J. Hone, and X. Y. Zhu, Optical generation of high carrier densities in 2D semiconductor heterobilayers, *Sci. Adv.* **5**, eaax0145 (2019).
- [18] H. Zhu, J. Wang, Z. Gong, Y. D. Kim, J. Hone, and X. Y. Zhu, Interfacial charge transfer circumventing momentum mismatch at two-dimensional van der Waals heterojunctions, *Nano Lett.* **17**, 3591 (2017).
- [19] S. Fu, I. du Fossé, X. Jia, J. Xu, X. Yu, H. Zhang, W. Zheng, S. Krasel, Z. Chen, Z. M. Wang *et al.*, Long-lived charge separation following pump-wavelength-dependent ultrafast charge transfer in graphene/WS<sub>2</sub> heterostructures, *Sci. Adv.* **7**, eabd9061 (2021).
- [20] N. Huo, J. Kang, Z. Wei, S.-S. Li, J. Li, and S.-H. Wei, Novel and enhanced optoelectronic performances of multilayer MoS<sub>2</sub>-WS<sub>2</sub> heterostructure transistors, *Adv. Funct. Mater.* **24**, 7025 (2014).
- [21] J. Hong, Z. Hu, M. Probert, K. Li, D. Lv, X. Yang, L. Gu, N. Mao, Q. Feng, L. Xie *et al.*, Exploring atomic defects in molybdenum disulphide monolayers, *Nat. Commun.* **6**, 6293 (2015).
- [22] H. Shu, Y. Li, X. Niu, and J. Wang, Greatly enhanced optical absorption of a defective MoS<sub>2</sub> monolayer through oxygen passivation, *ACS Appl. Mater. Interfaces* **8**, 13150 (2016).
- [23] J. Jiang, C. Ling, T. Xu, W. Wang, X. Niu, A. Zafar, Z. Yan, X. Wang, Y. You, L. Sun *et al.*, Defect engineering for modulating the trap states in 2D photoconductors, *Adv. Mater.* **30**, e1804332 (2018).
- [24] Y. Ouyang, Y. Zhou, Y. Zhang, Q. Li, and J. Wang, Double-edged roles of intrinsic defects in two-dimensional MoS<sub>2</sub>, *Trends Chem.* **4**, 451 (2022).
- [25] L. Li, R. Long, and O. V. Prezhdo, Why chemical vapor deposition grown MoS<sub>2</sub> samples outperform physical vapor deposition samples: Time-domain *ab initio* analysis, *Nano Lett.* **18**, 4008 (2018).
- [26] J. Jiang, Q. Zhang, A. Wang, Y. Zhang, F. Meng, C. Zhang, X. Feng, Y. Feng, L. Gu, H. Liu *et al.*, A facile and effective method for patching sulfur vacancies of WS<sub>2</sub> via nitrogen plasma treatment, *Small* **15**, e1901791 (2019).
- [27] A. Forster, S. Gemming, G. Seifert, and D. Tomanek, Chemical and electronic repair mechanism of defects in MoS<sub>2</sub> monolayers, *ACS Nano* **11**, 9989 (2017).
- [28] L. Li, Z. Qin, L. Ries, S. Hong, T. Michel, J. Yang, C. Salameh, M. Bechelany, P. Miele, D. Kaplan *et al.*, Role of sulfur vacancies and undercoordinated Mo regions in MoS<sub>2</sub> nanosheets toward the evolution of hydrogen, *ACS Nano* **13**, 6824 (2019).
- [29] L. Zhang, W. Chu, Q. Zheng, A. V. Benderskii, O. V. Prezhdo, and J. Zhao, Suppression of electron-hole recombination by intrinsic defects in 2D mono-elemental material, *J. Phys. Chem. Lett.* **10**, 6151 (2019).

- [30] G. Kresse and J. Furthmüller, Efficiency of *ab-initio* total energy calculations for metals and semiconductors using a plane-wave basis set, *Comp. Mater. Sci.* **6**, 15 (1996).
- [31] G. Kresse and J. Furthmüller, Efficient iterative schemes for *ab initio* total-energy calculations using a plane-wave basis set, *Phys. Rev. B* **54**, 11169 (1996).
- [32] C. Long, Y. Dai, Z.-R. Gong, and H. Jin, Robust type-II band alignment in Janus-MoSSe bilayer with extremely long carrier lifetime induced by the intrinsic electric field, *Phys. Rev. B* **99**, 115316 (2019).
- [33] J. P. Perdew, K. Burke, and M. Ernzerhof, Generalized gradient approximation made simple, *Phys. Rev. Lett.* **77**, 3865 (1996).
- [34] J. P. Perdew, Density-functional approximation for the correlation energy of the inhomogeneous electron gas, *Phys. Rev. B* **33**, 8822 (1986).
- [35] S. Grimme, Semiempirical GGA-type density functional constructed with a long-range dispersion correction, *J. Comput. Chem.* **27**, 1787 (2006).
- [36] M. Barbatti, Nonadiabatic dynamics with trajectory surface hopping method, *WIREs, Comput. Mol. Sci.* **1**, 620 (2011).
- [37] W. Chu, Q. Zheng, O. V. Prezhdo, J. Zhao, and W. A. Saidi, Low-frequency lattice phonons in halide perovskites explain high defect tolerance toward electron-hole recombination, *Sci. Adv.* **6**, eaaw7453 (2020).
- [38] J. C. Tully, Molecular dynamics with electronic transitions, *J. Chem. Phys.* **93**, 1061 (1990).
- [39] Y. Wang, Y. Shi, C. Zhao, Q. Zheng, and J. Zhao, Photogenerated carrier dynamics at the anatase/rutile TiO<sub>2</sub> interface, *Phys. Rev. B* **99**, 165309 (2019).
- [40] A. V. Akimov and O. V. Prezhdo, The PYXAID program for non-adiabatic molecular dynamics in condensed matter systems, *J. Chem. Theory Comput.* **9**, 4959 (2013).
- [41] H. M. Jaeger, S. Fischer, and O. V. Prezhdo, Decoherence-induced surface hopping, *J. Chem. Phys.* **137**, 22A545 (2012).
- [42] J. Liu, X. Zhang, and G. Lu, Excitonic effect drives ultrafast dynamics in van der Waals heterostructures, *Nano Lett.* **20**, 4631 (2020).
- [43] K. Kośmider and J. Fernández-Rossier, Electronic properties of the MoS<sub>2</sub>-WS<sub>2</sub> heterojunction, *Phys. Rev. B* **87**, 075451 (2013).
- [44] Q. Zheng, Y. Xie, Z. Lan, O. V. Prezhdo, W. A. Saidi, and J. Zhao, Phonon-coupled ultrafast interlayer charge oscillation at van der Waals heterostructure interfaces, *Phys. Rev. B* **97**, 205417 (2018).
- [45] Y. Tian, Q. Zheng, and J. Zhao, Tensile strain-controlled photo-generated carrier dynamics at the van der Waals heterostructure interface, *J. Phys. Chem. Lett.* **11**, 586 (2020).
- [46] See Supplemental Material at <http://link.aps.org/supplemental/10.1103/PhysRevB.108.165428> for details of atomic structures, defect formation energy, charge densities and NAMD data of MoS<sub>2</sub>/WS<sub>2</sub> heterostructure with and without S vacancies, and band structure of TMD heterostructures without S vacancies and after O<sub>2</sub> repaired S-group vacancies.
- [47] J. He, W. H. Fang, and R. Long, Unravelling the effects of oxidation state of interstitial iodine and oxygen passivation on charge trapping and recombination in CH<sub>3</sub>NH<sub>3</sub>PbI<sub>3</sub> perovskite: A time-domain *ab initio* study, *Chem. Sci.* **10**, 10079 (2019).
- [48] H. Chen, X. Wen, J. Zhang, T. Wu, Y. Gong, X. Zhang, J. Yuan, C. Yi, J. Lou, P. M. Ajayan *et al.*, Ultrafast formation of interlayer hot excitons in atomically thin MoS<sub>2</sub>/WS<sub>2</sub> heterostructures, *Nat. Commun.* **7**, 12512 (2016).
- [49] J. Yang, S. Jiang, J. Xie, H. Jiang, S. Xu, K. Zhang, Y. Shi, Y. Zhang, Z. Zeng, G. Fang *et al.*, Identifying the intermediate free-carrier dynamics across the charge separation in monolayer MoS<sub>2</sub>/ReSe<sub>2</sub> heterostructures, *ACS Nano* **15**, 16760 (2021).
- [50] V. R. Policht, M. Russo, F. Liu, C. Trovatiello, M. Maiuri, Y. Bai, X. Zhu, S. Dal Conte, and G. Cerullo, Dissecting interlayer hole and electron transfer in transition metal dichalcogenide heterostructures via two-dimensional electronic spectroscopy, *Nano Lett.* **21**, 4738 (2021).
- [51] J. He, W. H. Fang, R. Long, and O. V. Prezhdo, Superoxide/peroxide chemistry extends charge carriers' lifetime but undermines chemical stability of CH<sub>3</sub>NH<sub>3</sub>PbI<sub>3</sub> exposed to oxygen: Time-domain *ab initio* analysis, *J. Am. Chem. Soc.* **141**, 5798 (2019).
- [52] R. Sarkar, M. Habib, S. Pal, and O. V. Prezhdo, Tuning charge transfer and recombination in exTTF/CNT nanohybrids by choice of chalcogen: A time-domain density functional analysis, *J. Appl. Phys.* **129**, 025501 (2020).
- [53] J. Meng, J. Wang, J. Wang, Q. Li, and J. Yang,  $\beta$ -SnS/GaSe heterostructure: A promising solar-driven photocatalyst with low carrier recombination for overall water splitting, *J. Mater. Chem. A* **10**, 3443 (2022).
- [54] Y. Wei, M. V. Tokina, A. V. Benderskii, Z. Zhou, R. Long, and O. V. Prezhdo, Quantum dynamics origin of high photocatalytic activity of mixed-phase anatase/rutile TiO<sub>2</sub>, *J. Chem. Phys.* **153**, 044706 (2020).
- [55] M. Amani, D.-H. Lien, D. Kiriya, J. Xiao, A. Azcatl, J. Noh, S. R. Madhupathy, R. Addou, K. C. Santosh, M. Dubey *et al.*, Near-unity photoluminescence quantum yield in MoS<sub>2</sub>, *Science* **350**, 1065 (2015).
- [56] S. Mignuzzi, A. J. Pollard, N. Bonini, B. Brennan, I. S. Gilmore, M. A. Pimenta, D. Richards, and D. Roy, Effect of disorder on Raman scattering of single-layer, *Phys. Rev. B* **91**, 195411 (2015).
- [57] T. X. Huang, X. Cong, S. S. Wu, K. Q. Lin, X. Yao, Y. H. He, J. B. Wu, Y. F. Bao, S. C. Huang, X. Wang *et al.*, Probing the edge-related properties of atomically thin MoS<sub>2</sub> at nanoscale, *Nat. Commun.* **10**, 5544 (2019).
- [58] R. Long, M. Guo, L. Liu, and W. Fang, Nonradiative relaxation of photoexcited black phosphorus is reduced by stacking with MoS<sub>2</sub>: A time domain *ab initio* study, *J. Phys. Chem. Lett.* **7**, 1830 (2016).
- [59] Z. Zhou, X. Niu, Y. Zhang, and J. Wang, Janus MoSSe/WSeTe heterostructures: A direct Z-scheme photocatalyst for hydrogen evolution, *J. Mater. Chem. A* **7**, 21835 (2019).

*Correction:* Labels indicating first and second corresponding authors were missing from the byline footnotes and have been inserted.